Computing a Class of Blow-up Solutions for the Navier-Stokes Equations

C. BOLDRIGHINI[1], S. FRIGIO[2], P. MAPONI[2], A. PELLEGRINOTTI[3]

[1]Istituto Nazionale di Alta Matematica (INdAM), Gruppo Nazionale per la Fisica Matematica (GNFM)
Università di Roma La Sapienza
Piazzale Aldo 2 Moro, 00185 Rome
ITALY

[2]Scuola di Scienze e Tecnologie
Università di Camerino
62032 Camerino (MC)
ITALY

[3]Dipartimento di Matematica e Fisica
Università di Roma Tre
Largo S. Leonardo Murialdo 1, 00146 Rome
ITALY

Abstract: The three-dimensional incompressible Navier-Stokes equations play a fundamental role in a large number of applications to fluid motions, and a large amount of theoretical and experimental studies were devoted to it. Our work is in the context of the Global Regularity Problem, i.e., whether smooth solutions in the whole space $\mathbb{R}^3$ can become singular ("blow-up") in a finite time. The problem is still open and also has practical importance, as the singular solutions would describe new phenomena. Our work is mainly inspired by a paper of Li and Sinai, who proved the existence of a blow-up for a class of smooth complex initial data. We present a study by computer simulations of a larger class of complex solutions and also of a related class of real solutions, which is a natural candidate for evidence of a blow-up. The numerical results show interesting features of the solutions near the blow-up time. They also show some remarkable properties for the real flows, such as a sharp increase of the total enstrophy and a concentration of high values of velocities and vorticity in small regions.

Key-Words: Navier-Stokes equations, Blow-up, Global Regularity Problem, Numerical solution, Fluid dynamics

Received: June 17, 2023. Revised: May 16, 2024. Accepted: July 11, 2024. Published: August 8, 2024.

1 Introduction

Fluid dynamics studies fluid motion and its interaction with the environment, such as solid bodies and other fluids. It has a wide variety of applications: calculating forces and moments, [1], determining the mass flow rate of oil through pipelines, [2], forecasting weather patterns, [3], designing aircrafts, [4], and turbine machines, [5], manage renewable energy sources, [6], [7], optimize processes in nutrition science, [8], [9], [10], [11], only to mention a few. The relevance of the applications stimulated an intense study of fluid dynamics from different points of view, from approximation and computational methods to obtain particular solutions to theoretical frameworks providing general properties of fluid dynamics models.

The incompressible Navier-Stokes equations describe the evolution of the flow velocity and pressure and they may well be considered the main model of fluid dynamics, [12]. We restrict our attention to flows in the whole space $\mathbb{R}^3$ with no boundary conditions. In spite of great efforts, important properties of the model remain to be established by the scientific research. The Global Regularity Problem (GRP), i.e., the problem whether smooth solutions in absence of forcing can become singular at a finite time, is still open and in the list of the Clay millennium prize, [13]. In the context of well definitness, [14], proved a global weak existence theorem and a uniqueness and regularity theorem only for finite times. The interest of possible singularities in the solution is that they would describe sudden concentrations of energy in a finite region (as it happens in tornadoes or hurricanes); in fact, the main features of the possible finite-time singularities ("blow-up"), are the divergence of the total enstrophy, [12], and the divergence at some point of the absolute value of the velocity, [15]. We note that the study of GRP is an extremely active field of study, where the Navier-Stokes equations is analysed theretically and numerically, see [16], [17], [18], [19], [20], [21].

Recently, [22], introduced a new approach to the study of incompressible Navier-Stokes equations. They considered the integral formulation of the equations in Fourier transform space for a particular class of initial data corresponding to complex solutions,

and could prove a finite-time blow-up by a renormalization group method. Following this initial contribution, several papers shed light on the properties of the solutions by theoretical studies, [23], and by computer simulations, [24], [25]. In this paper, we describe the integral formulation of the Navier-Stokes equations, and the numerical approximation scheme for their simulation. We then report the main results obtained by a high performance computing code, both for some complex and some related real solutions.

The organization of the paper is as follows. In the next section, we provide a detailed derivation of the integral formulation of the Navier-Stokes equations in the Fourier transform space. In section 3, we describe the approximation scheme of the integral equation arising from the Navier-Stokes equations. In section 4, we show the results obtained in numerical experiments with the complex and real solutions of the Navier-Stokes equations. In section 5, we provide some conclusions and final remarks.

2 Integral formulation of the Navier-Stokes equations

We consider the initial value problem for the incompressible Navier-Stokes equations in the whole space with no boundary conditions:

$$\frac{\partial \mathbf{u}}{\partial t} + \sum_{j=1}^{3} u_j \frac{\partial \mathbf{u}}{\partial x_j} = \Delta \mathbf{u} - \nabla p, \quad \mathbf{x} = (x_1, x_2, x_3)^t \in \mathbb{R}^3,\ t > 0, \tag{1}$$

$$\nabla^t \mathbf{u} = 0,\ \mathbf{x} \in \mathbb{R}^3,\ t > 0, \tag{2}$$

$$\mathbf{u}(\mathbf{x}, 0) = \mathbf{u}_0(\mathbf{x}),\ \mathbf{x} \in \mathbb{R}^3, \tag{3}$$

where $\mathbf{u} = (u_1, u_2, u_3)^t$ is the velocity vector, p is the pressure, ∇ denotes the gradient operator, ∇^t denotes the divergence operator, Δ denotes the Laplacian operator, and $\mathbf{u}_0$ is the initial velocity of the fluid. The viscosity in (1) is $\nu = 1$, which can be always obtained by space scaling, since no boundaries are prescribed.

We define the Fourier transform $\hat{\mathbf{u}}$ of $\mathbf{u}$ as follows:

$$\hat{\mathbf{u}}(\mathbf{k}, t) = (\mathcal{F}\mathbf{u}(\cdot, t))(\mathbf{k}) = \frac{1}{(2\pi)^3} \int_{\mathbb{R}^3} \mathbf{u}(\mathbf{x}, t) e^{-\imath \langle \mathbf{k}, \mathbf{x} \rangle} d\mathbf{x},\ \mathbf{k} \in \mathbb{R}^3,$$

where $\langle \cdot, \cdot \rangle$ is the scalar product in $\mathbb{R}^3$. The integral formulation considers the function $\mathbf{v}(\mathbf{k}, t) = \imath \hat{\mathbf{u}}(\mathbf{k}, t)$, so from standard arguments on Fourier transform theory we have:

$$\mathbf{u}(\mathbf{x}, t) = -\imath (\mathcal{F}^{-1} \mathbf{v}(\cdot, t))(\mathbf{x}) = -\imath \int_{\mathbb{R}^3} \mathbf{v}(\mathbf{k}, t) e^{\imath \langle \mathbf{k}, \mathbf{x} \rangle} d\mathbf{k}. \tag{4}$$

Let $f, g : \mathbb{R} \to \mathbb{R}$ be two regular functions, we remind two well-known properties of the Fourier transform:

$$\mathcal{F}(Df) = ik\hat{f}, \tag{5}$$

$$\mathcal{F}(fg) = \hat{f} * \hat{g}, \tag{6}$$

where Df denotes the derivative of f and

$$(f * g)(x) = \int_{\mathbb{R}} f(x') g(x - x') dx' \tag{7}$$

denotes the convolution integral. We note that from (5), (6), the symmetry of the convolution integral and the definition of function $\mathbf{v}$ we have

$$\left(\mathcal{F} \left(\sum_{j=1}^{3} u_j(\cdot, t) \frac{\partial \mathbf{u}}{\partial x_j}(\cdot, t) \right) \right) (\mathbf{k}) = \left(\sum_{j=1}^{3} \hat{u}_j(\cdot, t) * (\imath k_j \hat{\mathbf{u}}(\cdot, t)) \right) (\mathbf{k}) = \int_{\mathbb{R}^3} \sum_{j=1}^{3} v_j(\mathbf{k} - \mathbf{k}', t) \left(\imath k'_j \mathbf{v}(\mathbf{k}', t) \right) d\mathbf{k}' = -\imath \int_{\mathbb{R}^3} \langle \mathbf{v}(\mathbf{k} - \mathbf{k}', t), \mathbf{k}' \rangle \mathbf{v}(\mathbf{k}', t) d\mathbf{k}'. \tag{8}$$

We apply the Fourier transform to the Navier-Stokes equations (1), and from relations (5)-(8) we obtain

$$\frac{\partial \mathbf{v}(\mathbf{k}, t)}{\partial t} + \|\mathbf{k}\|^2 \mathbf{v}(\mathbf{k}, t) = \int_{\mathbb{R}^3} \langle \mathbf{v}(\mathbf{k} - \mathbf{k}', t), \mathbf{k}' \rangle \mathbf{v}(\mathbf{k}', t) d\mathbf{k}' - \imath \mathbf{k} \hat{p}(\mathbf{k}, t), \tag{9}$$

where $\hat{p}$ is the Fourier transform of p. From the incompressibility equation (2) we see that $\mathbf{u}$ is a rotation (or solenoidal) field, so that in the Fourier space:

$$\left(\mathcal{F} \left(\nabla^t \mathbf{u}(\cdot, t) \right) \right) (\mathbf{k}) = \imath \langle \mathbf{k}, \hat{\mathbf{u}}(\mathbf{k}, t) \rangle = 0. \tag{10}$$

So, in the Fourier space, the incompressibility equation (2) reduces to the orthogonality of $\hat{\mathbf{u}}(\mathbf{k}, t)$ to $\mathbf{k}$, hence, the projectior on the subspace of the rotation fields coincides with the projector $P_{\mathbf{k}}$ on the subspace of vectors orthogonal to $\mathbf{k}$, so that for a generic vector $\mathbf{w} \in \mathbb{R}^3$ it is defined as:

$$P_{\mathbf{k}} \mathbf{w} = \mathbf{w} - \frac{\langle \mathbf{w}, \mathbf{k} \rangle}{\|\mathbf{k}\|^2} \mathbf{k}. \tag{11}$$

We can easily see that $P_{\mathbf{k}}$ has no effect on the function $\hat{\mathbf{u}}(\mathbf{k}, t)$, that is $P_{\mathbf{k}} \hat{\mathbf{u}}(\mathbf{k}, t) = \hat{\mathbf{u}}(\mathbf{k}, t)$; on the other hand, it cancels the term $\imath \mathbf{k} \hat{p}(\mathbf{k}, t)$ in formula (9), in fact $P_{\mathbf{k}} \mathbf{k} = \mathbf{0}$. Thus, when we apply $P_{\mathbf{k}}$ to equation

(9) we get

$$\frac{\partial \mathbf{v}(\mathbf{k},t)}{\partial t} + \|\mathbf{k}\|^2 \mathbf{v}(\mathbf{k},t) = \int_{\mathbb{R}^3} \langle \mathbf{v}(\mathbf{k}-\mathbf{k}',t), \mathbf{k}' \rangle P_{\mathbf{k}} \mathbf{v}(\mathbf{k}',t) d\mathbf{k}'. \quad (12)$$

We multiply both sides of (12) by $e^{t\|\mathbf{k}\|^2}$ obtaining on the right the time-derivative of $e^{t\|\mathbf{k}\|^2}\mathbf{v}(\mathbf{k},t)$ and, by a time integration, the following equation:

$$\mathbf{v}(\mathbf{k},t) = e^{-t\|\mathbf{k}\|^2}\mathbf{v}_0(\mathbf{k}) + \int_0^t e^{-(t-s)\|\mathbf{k}\|^2}\mathbf{C}(\mathbf{k},s;\mathbf{v})ds, \quad (13)$$

where

$$\mathbf{C}(\mathbf{k},s;\mathbf{v}) = \int_{\mathbb{R}^3} \langle \mathbf{v}(\mathbf{k}-\mathbf{k}',s), \mathbf{k}' \rangle P_{\mathbf{k}} \mathbf{v}(\mathbf{k}',s) d\mathbf{k}', \quad (14)$$

is a convolution integral and the initial data $\mathbf{v}_0$ are the Fourier transform of the data $\mathbf{u}_0$ in (3).

Equation (13) provides the integral formulation of the Navier-Stokes equations. We note that the study of Li and Sinai considers real solutions of this equation, which correspond in general to complex solutions of the original Navier-Stokes equations (1). However, if the initial data $\mathbf{v}_0$, and hence the solution of equation (13), is antisymmetric, (i.e. $\mathbf{v}(-\mathbf{k},t) = -\mathbf{v}(\mathbf{k},t)$), then the solution in the physical space is real and describes a fluid flow.

3 The approximation scheme

We consider the following problem: given $\mathbf{v}_0$, compute a numerical approximation $\mathbf{V}(\mathbf{k},t)$ of $\mathbf{v}(\mathbf{k},t)$ for $\mathbf{k} \in R \subset \mathbb{R}^3$, and $t \in T \subset [0,\bar{t}]$, where R, T are suitable discrete sets.

We note that equation (13) has a structure of a Volterra integral equation in the time variable and a Fredholm integral equation in the space (conjugate) variables, when a suitable truncation of $\mathbb{R}^3$ is considered. So, roughly speaking, the proposed approximation is based on a time-marching scheme where in each step an iterative solution of the nonlinear Fredholm equation is computed, see [26], for a general introduction to numerical approximation schemes for integral equations.

We consider a uniform partition $T = \{t_n = \delta_t n, n = 0,1,\ldots,N\}$ of the interval $[0,\bar{t}]$ with step size $\delta_t = \frac{\bar{t}}{N}$. Knowing the solution $\mathbf{v}(\mathbf{k},t_n)$, $\mathbf{k} \in \mathbb{R}^3$ at time t_n, we can formally compute $\mathbf{v}(\mathbf{k},t_{n+1})$ for $\mathbf{k} \in \mathbb{R}^3$ by using the rectangle quadrature formula

$$\begin{aligned}\mathbf{v}(\mathbf{k},t_{n+1}) &= e^{-\delta_t\|k\|^2}\mathbf{v}(\mathbf{k},t_n) + \int_{t_n}^{t_{n+1}} e^{-\|k\|^2(t_{n+1}-s)}\mathbf{C}(\mathbf{k},s;\mathbf{v})ds \\ &\approx e^{-\delta_t\|k\|^2}\mathbf{v}(\mathbf{k},t_n) + \delta_t e^{-\delta_t\|k\|^2}\mathbf{C}(\mathbf{k},t_n;\mathbf{v}), \quad (15)\end{aligned}$$

or by using the trapezoidal quadrature formula

$$\mathbf{v}(\mathbf{k},t_{n+1}) \approx e^{-\delta_t\|k\|^2}\mathbf{v}(\mathbf{k},t_n) + \frac{\delta_t}{2}\Big(e^{-\delta_t\|k\|^2}\mathbf{C}(\mathbf{k},t_n;\mathbf{v}) + \mathbf{C}(\mathbf{k},t_{n+1};\mathbf{v})\Big). \quad (16)$$

For the discretization of the spatial variables, we suppose that, for $t \in T$, $\mathbf{v}(\mathbf{k},t)$ is negligible if $\mathbf{k}$ is outside the parallelepiped $[a_1,b_1] \times [a_2,b_2] \times [a_3,b_3]$, and consider a uniform mesh on it: $R = \{\mathbf{k}_{i,j,l} = (a_1 + \delta_1 i, a_2 + \delta_2 j, a_3 + \delta_3 l)^t,\ i = 0,1,\ldots,I,\ j = 0,1,\ldots,J,\ l = 0,1,\ldots,L\}$ with step sizes $\delta_1 = \frac{b_1-a_1}{I}$, $\delta_2 = \frac{b_2-a_2}{J}$, $\delta_3 = \frac{b_3-a_3}{L}$, respectively. Let $\mathbb{I}$ be the set of indices defined in R, the approximation $\mathbf{V}_n = \{\mathbf{v}_{i,j,l,n}, (i,j,l) \in \mathbb{I}\}$ of $\mathbf{v}(\mathbf{k}_{i,j,l},t_n)$, $\mathbf{k}_{i,j,l} \in R$, $t_n \in T$ can be computed by formulas (15) and (16) applying the trapezoidal quadrature formula with nodes R, that is

$$\mathbf{v}_{i,j,l,n+1} = e^{-\delta_t\|\mathbf{k}_{i,j,l}\|^2}\mathbf{v}_{i,j,l,n} + \delta_t e^{-\delta_t\|\mathbf{k}_{i,j,l}\|}\tilde{\mathbf{c}}(i,j,l,\mathbf{V}_n), \quad (17)$$

$$\mathbf{v}_{i,j,l,n+1} = e^{-\delta_t\|\mathbf{k}_{i,j,l}\|^2}\mathbf{v}_{i,j,l,n} + \frac{\delta_t}{2}\Big(e^{-\delta_t\|\mathbf{k}_{i,j,l}\|^2}\tilde{\mathbf{c}}(i,j,l,\mathbf{V}_n) + \tilde{\mathbf{c}}(i,j,l,\mathbf{V}_{n+1})\Big) \quad (18)$$

where

$$\tilde{\mathbf{c}}(i,j,l,\mathbf{V}_m) = \sum_{(p,q,r)\in\mathbb{I}} W_{p,q,r}\langle \mathbf{k}_{i,j,l}, \mathbf{v}(\mathbf{k}_{i,j,l} - \mathbf{k}_{p,q,r}, t_m)\rangle \cdot P_{\mathbf{k}_{i,j,l}}\mathbf{v}_{p,q,r,m}, \quad (19)$$

is a discrete convolution term, and $W_{p,q,r}$, $(p,q,r) \in \mathbb{I}$ are the trapezoidal quadrature weights. We note that the function $\tilde{\mathbf{c}}$ defined in (19) can be efficiently computed by using the FFT algorithm.

Formula (17) gives an explicit Euler discretization scheme for equation (13), in fact it explicitely gives variables $\mathbf{V}_{n+1}$ in terms of $\mathbf{V}_n$. Formula (18) gives an implicit discretization scheme for equation (13), where variables $\mathbf{V}_{n+1}$ can be computed from $\mathbf{V}_n$ by solving a nonlinear equation; this last scheme is usually called Crank-Nicolson scheme. By a usual strategy, these schemes are jointly used to profitably exploit the stability features of the implicit methods and, in the particular case of the Crank-Nicolson scheme, also to obtain a second order accuracy with respect to the discretization steps in the time and spatial variables.

Algorithm 1 *Let T and R be the aforementioned discretization sets for the time variable and space variables, respectively; let $n = 0,1,\ldots,N$ and $\mathbb{I}$ the corresponding sets of indices. Let $tol > 0$ and $\overline{\nu} \in \mathbb{N}$ be given tolerances. Let $\mathbf{V}_0 = \{\mathbf{v}(\mathbf{k}_{i,j,l},0),\ (i,j,l) \in \mathbb{I}\}$.*

Compute the approximation $\mathbf{V}_n$, $n = 1, 2, \ldots, N$ *of the solution of (13) at* $t \in T$ *by performing the following steps:*

i) For $n = 0, 1, \ldots, N-1$,

ii) $\mathbf{v}^{(0)}_{i,j,l,n+1} = e^{-\delta_t \|\mathbf{k}_{i,j,l}\|^2} \mathbf{v}_{i,j,l,n} + \delta_t e^{-\delta_t \|\mathbf{k}_{i,j,l}\|^2} \cdot \tilde{\mathbf{c}}(i,j,l,\mathbf{V}_n)$, $(i,j,l) \in \mathbb{I}$

iii) $\nu = 0$,

iv) Repeat

v) $\nu = \nu + 1$,

vi) $\mathbf{v}^{(\nu)}_{i,j,l,n+1} = e^{-\delta_t \|\mathbf{k}_{i,j,l}\|^2} \mathbf{v}_{i,j,l,n} + \frac{\delta_t}{2}\Big(e^{-\delta_t \|\mathbf{k}_{i,j,l}\|^2} \tilde{\mathbf{c}}(i,j,l,\mathbf{V}_n) + \tilde{\mathbf{c}}(i,j,l,\mathbf{V}^{(\nu-1)}_{n+1})\Big)$, $(i,j,l) \in \mathbb{I}$,

vii) Until $\left\|\mathbf{V}^{(\nu)}_{n+1} - \mathbf{V}^{(\nu-1)}_{n+1}\right\| < tol$ *or* $\nu > \overline{\nu}$ *do*

viii) $\mathbf{V}_{n+1} = \mathbf{V}^{(\nu)}_{n+1}$.

We note that Algorithm 1 computes an initial approximation $\mathbf{V}^{(0)}_n$ of the solution at time t_n by using the Euler method (17) and recursively refines such initial guess by using the Crank-Nicolson method (18). This iterative process terminates when two consecutive solution vectors are sufficiently close or a maximum number of iterations is reached. Moreover, from standard arguments on Fourier transform theory, we have that the computational cost of term **C** in steps ii) and iv) can be considered linear in the number of variables in the arrays $\mathbf{V}_n$.

4 Numerical experiment

We describe some results of a numerical experiment performed by Algorithm 1, implemented in FORTRAN 90. The MPI software library, [27], is used to take advantage of parallel computing architectures to enhance the performance of the computational code. The 2Decomp&FFT library, [28], is used to compute the discrete convolution term $\tilde{\mathbf{c}}$ in (19).

The results reported in this section have two main aims: i) showing the accuracy of Algorithm 1, ii) underlying some useful properties of the solutions of equation (13); they are reported in two sections. Section 4.1 analyses the accuracy of Algorithm 1; in particular, we consider one set of initial data and compare the numerical solutions obtained by using different discretization parameters. In section 4.2 we consider different initial data by highlighting their blow-up properties.

4.1 Accuracy of the discretization scheme

Let A be a positive constant, and $B \subset \mathbb{R}^3$ be the sphere of center $\mathbf{k}_0 = (0, 0, c)$ and radius $0 < r < |c|$, let

$$\mathbf{Y} = \frac{\mathbf{k} - \mathbf{k}_0}{\sqrt{|\mathbf{k}_0|}},$$

and

$$\mathbf{v}(\mathbf{k}, 0) = \begin{cases} -A\Big(Y_1, Y_2, -\frac{k_1 Y_1 + k_2 Y_2}{k_3}\Big)^t e^{-\frac{|\mathbf{Y}|^2}{2}}, \mathbf{k} \in B, \\ \mathbf{0}, \mathbf{k} \notin B. \end{cases} \tag{20}$$

In particular, we choose $c = 20$, $r = 17$, and A such that the energy of the initial data is

$$\frac{1}{2} \int_{\mathbb{R}^3} |\mathbf{v}(\mathbf{k}, 0)|^2 \, d\mathbf{k} = 200.$$

The discretization of (13) is obtained by using the same discretization step $\delta_k > 0$ along the three coordinate directions, i.e. $\delta_k = \delta_1 = \delta_2 = \delta_3$.

Table 1: Difference in the approximated solutions computed with different discretization steps δ_k: first row $\delta_k = 1, 0.5$, second row $\delta_k = 0.5, 0.25$; the results are computed by using the space interval $[-127, 127] \times [-127, 127] \times [-19, 1004]$, $\delta_t = 10^{-6}$ and they refer to the first time-iterate. The notation $x(y)$ stays for $x \cdot 10^y$.

δ_k	ϵ_1	ϵ_2	ϵ_3
1-0.5	$9.4(-7)$	$5.6(-9)$	$2.5(-7)$
0.5-0.25	$3.1(-8)$	$5.6(-9)$	$2.6(-8)$

Table 2: Difference in the approximated solutions computed with different discretization steps δ_t: first row $\delta_t = 10^{-6}, 0.5\,10^{-6}$, second row $\delta_t = 0.5\,10^{-6}, 0.25\,10^{-6}$; the results are computed by using the space interval $[-127, 127] \times [-127, 127] \times [-19, 1004]$, $\delta_k = 1$ and they refer to the first time-iterate. The notation $x(y)$ stays for $x \cdot 10^y$.

δ_t	ϵ_1	ϵ_2	ϵ_3
$1(-6) - 0.5(-6)$	$2.3(-7)$	$4.7(-17)$	$1.2(-11)$
$0.5(-6) - 0.25(-6)$	$1.2(-14)$	$1.2(-17)$	$5.7(-13)$

The numerical results show the difference between the approximated solutions computed by using different discretization parameters; more precisely, three points are considered: $\mathbf{k}_1 = (-2, 5, 22)^t$, $\mathbf{k}_2 = (10, -20, 18)^t$, $\mathbf{k}_3 = (-5, 10, 40^t)$, and the corresponding errors ϵ_l, $l = 1, 2, 3$ are reported. In particular, Table 1 shows the differences in the numerical solutions obtained with different spatial discretization

Table 3: Difference in the approximated solutions computed with different space intervals $[-63, 63] \times [-63, 63] \times [-19, 501]$, $[-127, 127] \times [-127, 127] \times [-19, 1004]$; the results are computed by using $\delta_k = 1$, $\delta_t = 10^{-6}$ and they refer to the time-iterate $n = 1, 195$. The notation $x(y)$ stays for $x \cdot 10^y$.

$Iterate$	ϵ_1	ϵ_2	ϵ_3
1	$2.3(-7)$	$7.9(-22)$	$8.0(-18)$
195	$3.3(-15)$	$5.6(-15)$	$3.2(-15)$

steps δ_k. Table 2 shows the differences in the numerical solutions obtained with different time discretization steps δ_t. Table 3 shows the differences in the numerical solutions obtained with different space intervals and at different time-iterates, i.e., $n = 1, 195$.

4.2 Blow-up properties of Li Sinai solutions

We analyse four cases. The first two are a complex flow with initial data given in section 4.1 (see formula (20)) and the corresponding case with antisymmetric initial data, which is a real solution of the problem (1)-(3). The other two cases are similar, except that in the initial data we set $c = 30$, so that the case with antisymmetric initial data is again a real solution of the problem (1)-(3).

In all cases, the results of the numerical simulations are described in terms of the following quantities: the total energy:

$$E(t) = \frac{1}{2} \int_{\mathbb{R}^3} |\mathbf{v}(\mathbf{k}, t)|^2 \, d\mathbf{k}, \tag{21}$$

the total enstrophy:

$$S(t) = \int_{\mathbb{R}^3} \|\mathbf{k}\|^2 \, |\mathbf{v}(\mathbf{k}, t)|^2 \, d\mathbf{k}, \tag{22}$$

and the marginal density for the enstrophy along the k_3 axis in $\mathbf{k}$-space;

$$S_3(k_3, t) = \int_{\mathbb{R}\times\mathbb{R}} \|\mathbf{k}\|^2 \, |\mathbf{v}(\mathbf{k}, t)|^2 \, dk_1 dk_2. \tag{23}$$

Observe that for the complex solutions there is a divergence of both energy and enstrophy, as predicted by the Li-Sinai theory. We note that with the initial data $\mathbf{v}_0$, centered along the k_3-axis, the support of the solution $\mathbf{v}$ of (13) extends along the k_3 axis, and the features of the blow-up are well described by the function S_3.

As already mentioned, the first example considers the initial data (20) in section 4.1. The numerical results are computed in the space interval

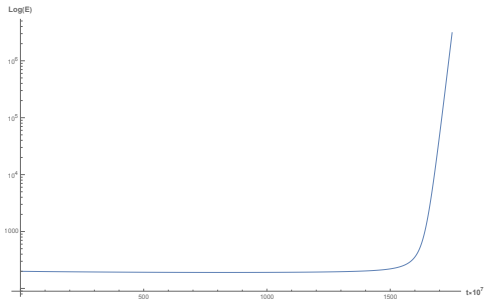

Fig. 1: First case: the total energy $E \quad (t)$, $t \in [0, 1550\ 10^{-7}]$ obtained with the initial data (20), i.e., a complex solution of (1)-(3) in the class of Li and Sinai solutions; the scale on the ordinate axis is logarithmic.

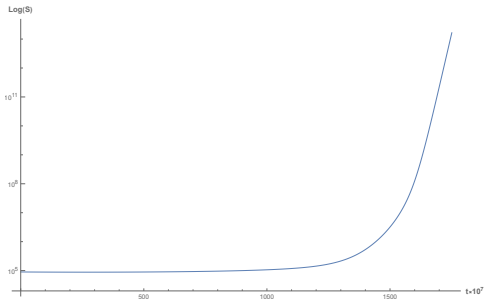

Fig. 2: First case: the total enstrophy $S \quad (t)$, $t \in [0, 1550\ 10^{-7}]$ obtained with the initial data (20), i.e., a complex solution of (1)-(3) in the class of Li and Sinai solutions; the scale on the ordinate axis is logarithmic.

$[-127, 127] \times [-127, 127] \times [-19, 2528]$, time interval $[0, 1550\ 10^{-7}]$, and discretization steps $\delta_1 = \delta_2 = \delta_3 = 1$, $\delta_t = 10^{-7}$. The results are reported in Figure 1, Figure 2, Figure 3. In particular, Figure 1 shows the plot of the total energy $E(t)$, $t \in [0, 1550\ 10^{-7}]$; Figure 2 shows the plot of the total enstrophy $S(t)$, $t \in [0, 1550\ 10^{-7}]$; Figure 3 shows the plot of the marginal density of the enstrophy along the k_3 axis in $\mathbf{k}$-space $S_3(k_3, t)$, $k_3 \in [-19, 2528]$ for three times near the blow-up, i.e. $t = 1450\ 10^{-7}$, $1500\ 10^{-7}$, $1530\ 10^{-7}$.

The results are quite satisfactory, in that they clearly show the blow-up properties of the complex solution of problem (1)-(3) under consideration. In particular, Figure 3 gives interesting information about the structure of the solution along the k_3-axis.

The second example considers an antisymmetric initial data of (13) providing a real solution of problem (1)-(3). More precisely, with the same notation introduced in section 4.1, we define:

$$\tilde{\mathbf{v}}(\mathbf{k}, 0) = \begin{cases} -A\left(Y_1, Y_2, -\frac{k_1 Y_1 + k_2 Y_2}{k_3}\right)^t e^{-\frac{|\mathbf{Y}|^2}{2}}, \mathbf{k} \in B, \\ \mathbf{0}, \mathbf{k} \notin B, \end{cases}$$

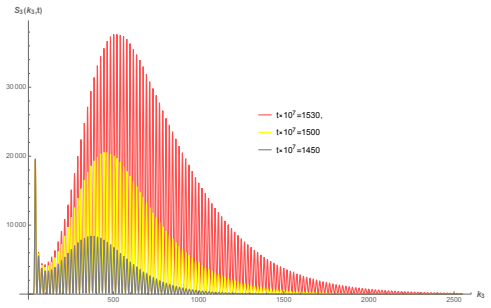

Fig. 3: First case: the marginal density for the enstrophy along the k_3 axis in **k**-space $S_3(k_3, t)$, $k_3 \in [-19, 2528]$ for three times near the blow-up, i.e. $t = 1450\ 10^{-7}$, $1500\ 10^{-7}$, $1530\ 10^{-7}$ obtained with the initial data (20), i.e., for a complex solution of (1)-(3) in the class of Li and Sinai solutions.

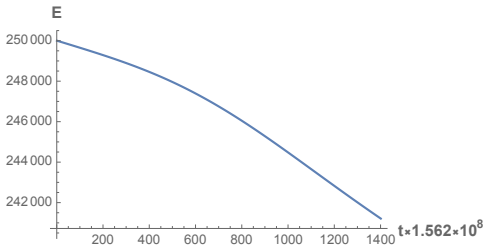

Fig. 4: Second case: the total energy $E \quad (t)$, $t \in [0, 2.19\ 10^{-5}]$ obtained with the initial data (24), i.e., for a real solution of (1)-(3).

$$\mathbf{v}(\mathbf{k}, 0) = \tilde{\mathbf{v}}(\mathbf{k}, 0) - \tilde{\mathbf{v}}(-\mathbf{k}, 0), \tag{24}$$

where again $c = 20$, $r = 17$, and A is such that the total initial energy $E(0) = 250000$.

The numerical results are computed by using the space interval $[-177,\ 177] \times [-177, 177] \times [-1200, 1200]$, with discretization steps $\delta_1 = \delta_2 = \delta_3 = 1$. The discretization step in time is $\delta_t = 1.5625\ \ 10^{-8}$ for a maximal time 1400, so that the resulting time interval is about $[0, 2.19\ \ 10^{-5}]$. The results are reported in Figure 4, Figure 5, Figure 6, Figure 13. In particular, Figure 4 shows the plot of the

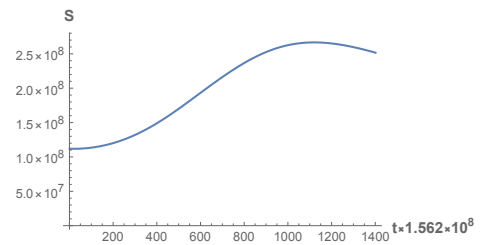

Fig. 5: Second case: the total enstrophy $S \quad (t)$, $t \in [0, 2.19\ 10^{-5}]$ obtained with the initial data (24), i.e., for a real solution of (1)-(3).

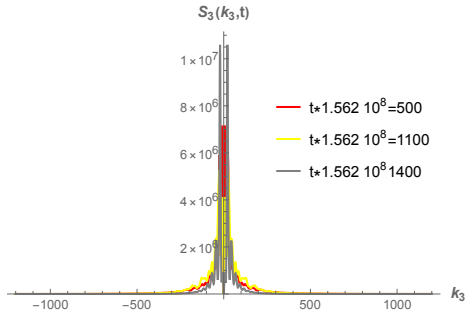

Fig. 6: Second case: the marginal density for the enstrophy along the k_3 axis in **k**-space $S_3(k_3, t_n)$, $k_3 \in [-1200, 1200]$ for three time-iterates near the maximum of the total enstrophy, i.e. $n = 500, 1100, 1400$ obtained with the initial data (24), i.e., for a real solution of (1)-(3).

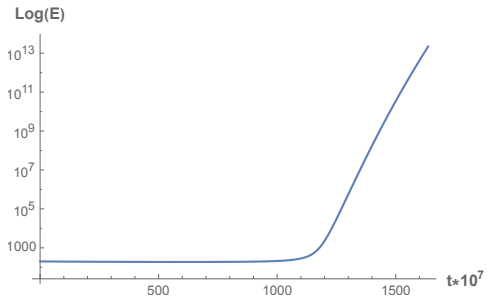

Fig. 7: Third case: the total energy $E \quad (t)$, $t \in [0, 1550\ 10^{-7}]$ obtained with the initial data (20) with $c = 30$, i.e., a complex solution of (1)-(3) in the class of Li and Sinai solutions; the scale on the ordinate axis is logarithmic.

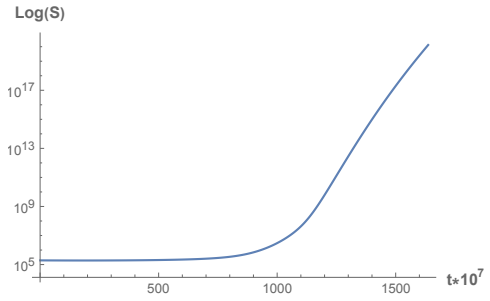

Fig. 8: Third case: the total enstrophy $S \quad (t)$, $t \in [0, 1550\ 10^{-7}]$ obtained with the initial data (20) with $c = 30$, i.e. a complex solution of (1)-(3) in the class of Li and Sinai solutions; the scale on the ordinate axis is logarithmic.

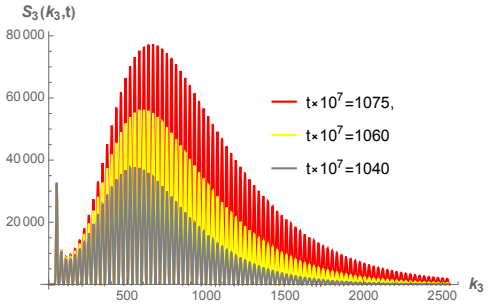

Fig. 9: T hird case: the marginal density for the enstrophy along the k_3 axis in **k**-space $S_3(k_3, t)$, $k_3 \in [-19, 2528]$ for three times near the blow-up, i.e. $t = 1040\ 10^{-7}, 1060\ 10^{-7}, 1075\ 10^{-7}$ obtained with the initial data (20) with $c = 30$, i.e., for a complex solution of (1)-(3) in the class of Li and Sinai solutions.

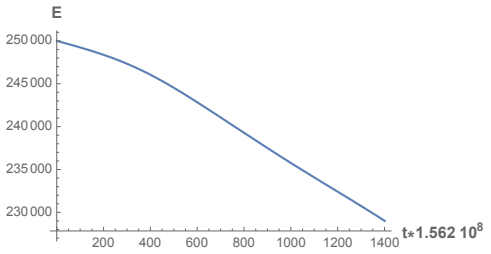

Fig. 10: Fourth case: the total energy $E\quad(t)$, $t \in [0, 2.19\ 10^{-5}]$ obtained with the initial data (24) with $c = 30$, i.e., for a real solution of (1)-(3).

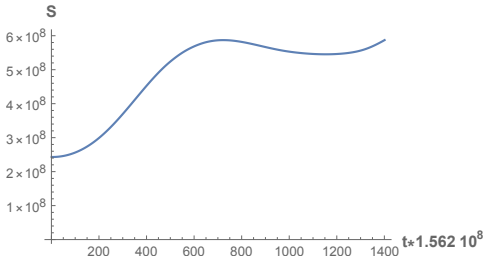

Fig. 11: Fourth case: the total enstrophy $S\quad(t)$, $t \in [0, 2.19\ 10^{-5}]$ obtained with the initial data (24) with $c = 30$, i.e., for a real solution of (1)-(3).

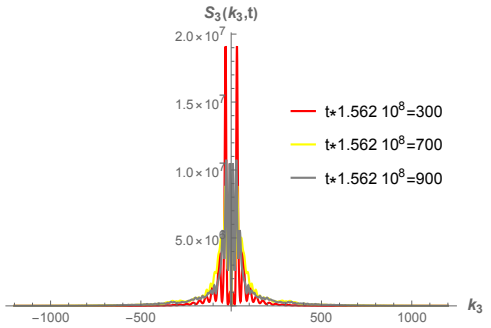

Fig. 12: Fourth case: the marginal density for the enstrophy along the k_3 axis in **k**-space $S_3(k_3, t_n)$, $k_3 \in [-1200, 1200]$ for three time-iterates near the maximum of the total enstrophy, i.e. $n = 300, 700, 900$ obtained with the initial data (24) with $c = 30$, i.e., for a real solution of (1)-(3).

total energy $E(t)$, $t \in [0, 2.19\ 10^{-5}]$, Figure 5 shows the plot of the total enstrophy $S(t)$, $t \in [0, 2.19\ 10^{-5}]$, and Figure 6 shows the plot of the marginal density of the enstrophy along the k_3 axis in **k**-space $S_3(k_3, t_n)$, $k_3 \in [-1200, 1200]$ for three time-iterates, i.e. $n = 500, 1100, 1400$.

The third example considers the initial data (20) in section 4.1, but with $c = 30$. The numerical results are computed by using the same discretization parameters of the first example. The results are reported in Figure 7, Figure 8, Figure 9; these figures are similar to the ones already described in the first example. However, the third example shows a more rapid blowup effect than the first one.

The fourth example considers the antisymmetric initial data (24), but with $c = 30$. The numerical results are computed by using the same discretization parameters of the second example. The results are reported in Figure 10, Figure 11, Figure 12; these figures are similar to the ones already described in the second example. Also for the real solution, the case $c = 30$ shows a higher increase in the total enstrophy than the case $c = 20$.

For the second example, Figure 13 shows a volume plot of the local energy $\|\mathbf{u}\|^2/2$ obtained by the inverse Fourier transform of the solution **v** of (13) at the final time iterate $n = 1400$. We note that, with the above grid in the **k**-space, **u** is defined for $\mathbf{x} \in [-\pi, \pi] \times [-\pi, \pi] \times [-\pi, \pi]$. We reported only the central part $[-50, 50] \times [-50, 50] \times [-100, 100]$ of the grid, which is the most significant, to highlight the structure of the solution: Figure 13 shows $\|\mathbf{u}(\mathbf{x}, t)\|^2$, $\mathbf{x} \in [-0.89, 0.89] \times [-0.89, 0.89] \times [-0.26, 0.26]$, $t = 2.19\ 10^{-5}$.

A statistical analysis of the properties of the solutions in the Li-SInai class would be very interesting, unfortunately this study has a prohibitive computa-

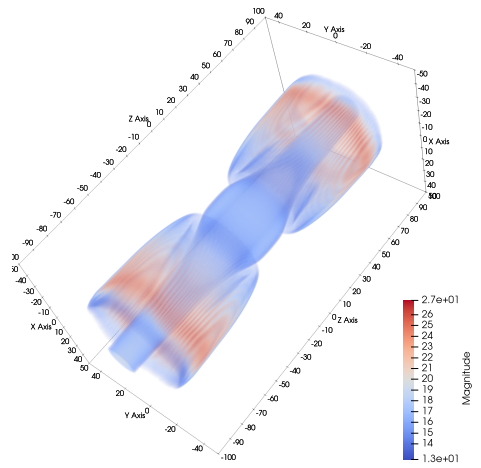

Figure 13: Second example: the local energy $\|\mathbf{u}\|^2/2$, in the subgrid $[-50, 50] \times [-50, 50] \times [-100, 100]$, at time iterate $n = 1400$, obtained with the initial data (24), i.e., for a real solution of (1)-(3).

tional cost since the numerical simulation of each case needs several tens of thousands of computation hours in tier0 supercomputers.

Also for the real case, in spite of the fact that there is no blow-up, the results are reliable and quite interesting. They provide evidence of a large increase in the total enstrophy that is related to a concentration of energy at some points along the k_3-axis.

Regarding the proposed numerical scheme, we can observe by a close analysis of the plot in Figure 6 some spurious effects due to the boundary of the computational domain. They are however quite small if we consider that the values at the boundary are obtained by multiplying the values of $\mathbf{v}$ by $\|\mathbf{k}\|^2$, and summing over k_1 and k_2. As the contribution of the boundary grows with time, the problem deserves further analysis to reduce as much as possible the effects.

The numerical results shown in sections 4.1, 4.2 are obtained by running the implementation code for Algorithm 1 under the system Joliot Curie – KNL, architecture BULL Sequana X1000, made available by the GENCI, [29], within the PRACE Project Access - Call 23, [30].

5 Conclusions

Our paper considers the incompressible Navier-Stokes equations in an equivalent formulation of an integral equation in Fourier space. An approximation scheme for this integral equation is proposed and some corresponding numerical results are presented.

The numerical simulations show that the approximation scheme is able to compute accurately the solution of the integral equation arising from the Navier-Stokes equations, even up to the blow-up time for some complex solutions, although, as expected, the accuracy is reduced when the solution support reaches the boundary of the computational domain. The results of the simulations also show interesting properties of the singular complex solutions, and, for the related real solutions provide evidence on the concentration of high velocity regions and on the increase of the total enstrophy. This study has considered the Li-Sinai solutions and analogous real solutions obtained by using antisymmetric initial data. As the initial data for the real solutions are axial symmetric with no swirl, it is well-known that the (real) solutions are regular for all times, [31]. The present computational framework can however be a useful tool to extend the Li and Sinai approach to a wider class of Navier-Stokes solutions. So, future studies have to extend the class of Li-Sinai solutions to initial data with non-zero swirl and generalize the previous results to this new class of solutions. Another interesting study is the organization of the presented computation tool in a computational fluid dynamc software, where the eventual boundary conditions can be easily treaded through an immersed boundary approach, [32].

Acknowledgment:
C. Boldrighini and A. Pellegrinotti are members of the Gruppo Nazionale Fisica Matematica-Istituto Nazionale di Alta Matematica (GNFM-INdAM). Pierluigi Maponi is a member of Gruppo Nazionale Calcolo Scientifico-Istituto Nazionale di Alta Matematica (GNCS-INdAM).
The computer simulations were performed at the Joliot Curie – KNL, architecture BULL Sequana X1000, made available by the GENCI, [29], within the PRACE Project Access - Call 23, [30].

References:

[1] Auton, T.R., The lift force on a spherical body in a rotational flow, *Journal of fluid mechanics* Vol. 183, 1987, pp. 199–218.

[2] Vegad, G.D. and Jana, A.K., Experimental and Computational Fluid Dynamics-Based Simulation of Oil-in-Water Emulsion Flow through a Pipeline. *Chemical Engineering & Technolog*, Vol. 46, 2023, pp. 1476-1484.

[3] Krishnamurti, T.N., "Numerical Weather Prediction". *Annual Review of Fluid Mechanics*, Vol. 27, 1995, pp. 95–225.

[4] Wang, Z. J., High-order computational fluid dynamics tools for aircraft design, *Philosophical transactions of the Royal Society of London.*

Series A: Mathematical, physical, and engineering sciences, Vol.372, 2022, p.1-18.

[5] Denton, J.D., Dawes, W.N., Computational fluid dynamics for turbomachinery design, *Proceedings of the Institution of Mechanical Engineers, Part C: Journal of Mechanical Engineering Science*, Vol.213, 1998, pp.107-124.

[6] Giacomini, J., Invernizzi, M.C., Maponi, P., Verdoya, M., Testing a model of flow and heat transfer for u-shaped geothermal exchangers. *Advances in Modelling and Analysis A*, Vol. 55, 2018, pp. 151–157.

[7] Egidi, N., Giacomini, J., Maponi, P., Inverse heat conduction to model and optimise a geothermal field. *Journal of Computational and Applied Mathematics*, Vol. 423, 2023, 114957.

[8] Giacomini, J., Khamitova, G., Maponi, P., Vittori, S., Fioretti, L., Water flow and transport in porous media for in-silico espresso coffee. *International Journal of Multiphase Flow*, Vol. 126, 2020, 103252.

[9] Egidi, N., Giacomini, J., Maponi, P., Perticarini, A., Cognigni, L., Fioretti, L., An advection–diffusion–reaction model for coffee percolation. *Computational and Applied Mathematics*, Vol. 41, 2022, 229.

[10] Angeloni, S., Giacomini, J., Maponi, P., Perticarini, A., Vittori, S., Cognigni, L., Fioretti, L., Computer Percolation Models for Espresso Coffee: State of the Art, Results and Future Perspectives. *Applied Sciences*, Vol. 13, 2023, 2688.

[11] Giacomini, J., Maponi, P., Perticarini, A., CMMSE: a reduced percolation model for espresso coffee. *Journal of Mathematical Chemistry*, Vol. 61, 2023, pp. 520–538.

[12] Temam, R., *Navier-Stokes Equations*, North Holland, 1979.

[13] Clay Mathematics Institute, *The Millennium Prize Problems*, accessed 22 July 2024, https://www.claymath.org/millennium-problems/

[14] Leray, J., Sur le mouvement d'un liquide visqueux emplissant l'espace. *Acta Math*, Vol. 63, 1934, pp. 193-248.

[15] Seregin, G., A Certain Necessary Condition of Potential Blow up for Navier-Stokes Equations. *Commun. Math. Phys.*, Vol. 312, 2012, pp. 833-845.

[16] T.Y. Hou, Y. Wang. 2024, Blowup Analysis for a Quasi-exact 1D Model of 3D Euler and Navier–Stokes, *Nonlinearity*, Vol. 37, 035001.

[17] T.Y. Hou, Potentially Singular Behavior of the 3D Navier–Stokes Equations, *Found Comput Math* Vol. 23, 2023, pp. 2251–2299.

[18] Okita, M. , On the blow-up criterion for the Navier–Stokes equations with critical time order, *Journal of Differential Equations*, Vol. 349, 2023, pp. 269-283,

[19] Tao, T., Quantitative bounds for critically bounded solutions to the Navier–Stokes equations, in *Nine mathematical challenges: an elucidation*, edited by A. Kechris et al., Proc. Sympos. Pure Math., Vol. 104, Amer. Math. Soc., Providence, RI, 2021, pp. 149–193.

[20] Wang, N., Hu, Y., Blowup of solutions for compressible Navier–Stokes equations with revised Maxwell's law, *Applied Mathematics Letters*, Vol. 103, 2020, 106221.

[21] T. Barker, 2023, 'Localized quantitative estimates and potential blow-up rates for Navier-Stokes equations', Siam Journal on Mathematical Analysis, vol. 55, no. 5, pp. 5221-5259. https://doi.org/10.1137/22M1527179

[22] Li, D., Sinai YA. G., Blowups of complex solutions of the 3D Navier-Stokes system and renormalization group method. *J. Eur. Math. Soc.*, Vol. 10, 2008, pp. 267-313.

[23] Boldrighini, C., Li, D., Sinai Ya., G., Complex singular solutions of the 3-d Navier-Stokes equations and related real solutions. *Journal of Statistical Physics*, Vol. 167, 2017, pp. 1-13.

[24] Boldrighini, C., Frigio, S., Maponi, P., On the blow-up of some complex solutions of the 3D Navier-Stokes Equations: theoretical predictions and computer simulation. *IMA Journal of Mathematical Physics*, Vol. 83, 2017, pp. 697-714.

[25] Boldrighini, C., Frigio, S., Maponi, P., Pellegrinotti, A., Sinai, Y.G., An Antisymmetric Solution of the 3D Incompressible Navier–Stokes Equations with "Tornado-Like" Behavior. *Journal of Experimental and Theoretical Physics*, Vol. 131, 2020, pp. 356–360.

[26] C.T.H. Baker, *The Numerical Treatment of Integral Equations*. Oxford Univ. Press, Oxford, 1977.

[27] MPI Forum, *MPI Forum*, accessed 22 July 2024, https://www.mpi-forum.org/

[28] Li, N., Laizet, S., 2DECOMP&FFT – A highly scalable 2D decomposition library and FFT interface, *Cray User Group 2010 conference*, Edinburgh, 2010.

[29] GENCI, *GENCI, HPC at the zervice of knowledge*, accessed 22 July 2024, https://www.genci.fr/en

[30] PRACE, *PRACE, Partnership for Advanced Computing in Europe*, accessed 22 July 2024, https://prace-ri.eu/

[31] Lei, Z., Zang, Q. Criticality of the axially symmetric Navier-Stokes equations, *Pacific Journal of Mathematics*, Vol. 289, 2017, pp. 169-187.

[32] Verzicco, R., Immersed Boundary Methods: Historical Perspective and Future Outlook, *Annual Review of Fluid Mechanics*, Vol. 55, 2023, pp. 129-155.

Contribution of Individual Authors to the Creation of a Scientific Article (Ghostwriting Policy)

The authors equally contributed in the present research, at all stages from the formulation of the problem to the final findings and solution.

Sources of Funding for Research Presented in a Scientific Article or Scientific Article Itself

No funding was received for conducting this study.

Conflicts of Interest

The authors have no conflicts of interest to declare that are relevant to the content of this article.